SANDIA REPORT

SAND88—1807 • UC—261
Unlimited Release
Printed August 1988

Strain Gauge Validation Experiments for the Sandia 34-Meter VAWT Test Bed

Herbert J. Sutherland

Prepared by
Sandia National Laboratories
Albuquerque, New Mexico 87185 and Livermore, California 94550
for the United States Department of Energy
under Contract DE-AC04-76DP00789

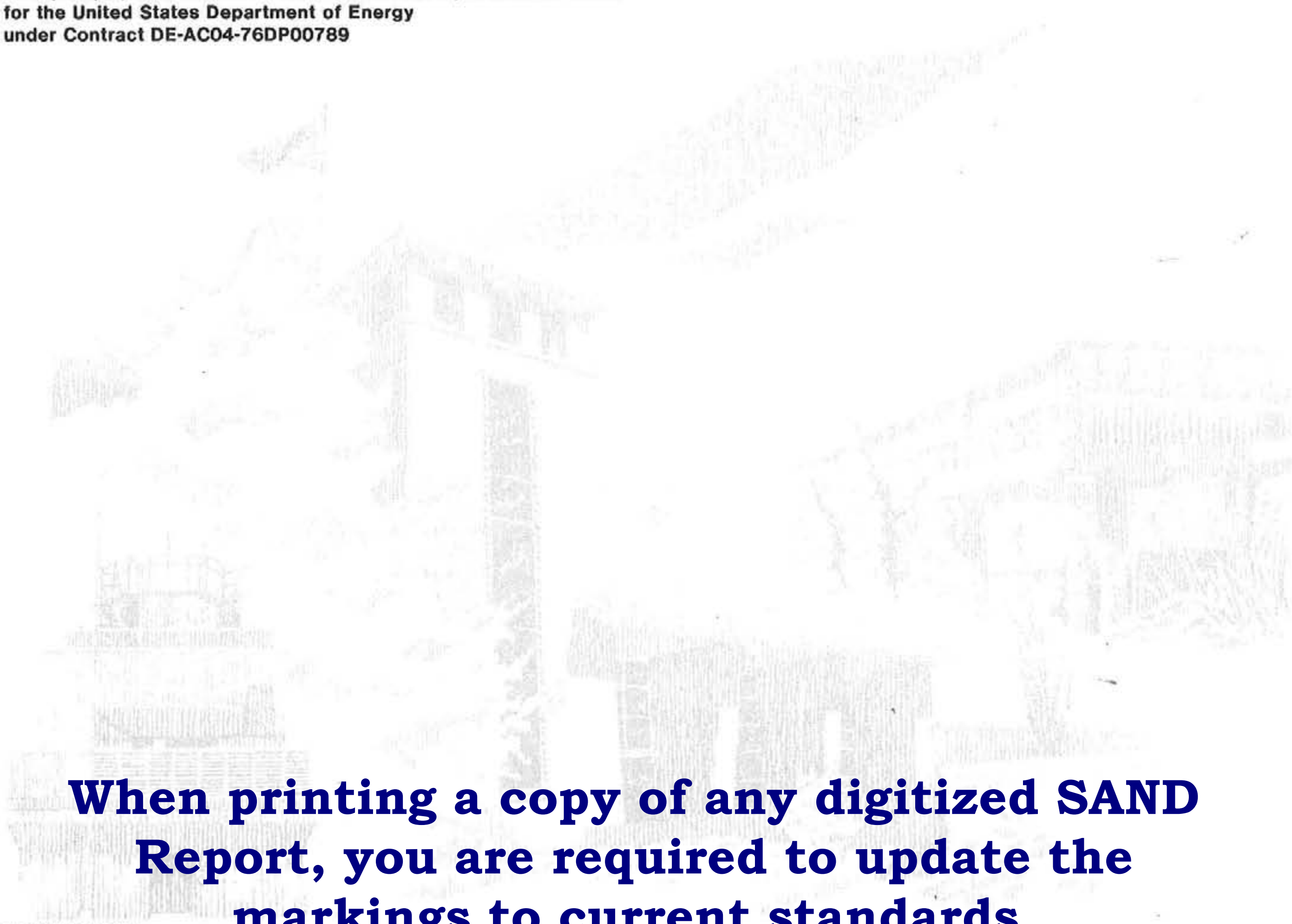

SF2900Q(8-81)

Issued by Sandia National Laboratories, operated for the United States Department of Energy by Sandia Corporation.

Printed in the United States of America
Available from
National Technical Information Service
U.S. Department of Commerce
5285 Port Royal Road
Springfield, VA 22161

NTIS price codes
Printed copy: A03
Microfiche copy: A01

Distribution
Category UC-261

SAND88-1807
Unlimited Release
Printed August 1988

STRAIN GAUGE VALIDATION EXPERIMENTS FOR THE SANDIA 34-METER VAWT TEST BED*

by

Herbert J. Sutherland

Wind Energy Research Division
Sandia National Laboratories
Albuquerque, New Mexico 87185

ABSTRACT

Sandia National Laboratories has erected a research oriented, 34-meter diameter, Darrieus vertical axis wind turbine near Bushland, Texas. This machine, designated the Sandia 34-m VAWT Test Bed, is equipped with a large array of strain gauges that have been placed at critical positions about the blades. This manuscript details a series of four-point bend experiments that were conducted to validate the output of the blade strain gauge circuits. The output of a particular gauge circuit is validated by comparing its output to "equivalent" gauge circuits (in this stress state) and to theoretical predictions. With only a few exceptions, the difference between measured and predicted strain values for a gauge circuit was found to be of the order of the estimated repeatability for the measurement system.

* This work was supported by the U. S. Department of Energy at Sandia National Laboratories under contract DE-AC04-76DP00789.

Table of Contents

Table of Contents (continued)

List of Tables

List of Figures

List of Appendices

INTRODUCTION

Sandia National Laboratories has erected a research-oriented, 34-meter diameter, Darrieus vertical axis wind turbine (VAWT) near Bushland, Texas, see Refs. 1 and 2. To meet current and future research needs, the turbine and its environment have been equipped with a large array of sensors, see Fig. 1, to monitor all aspects of the machine's performance. Current instrumentation includes 57 strain signals from the blades, 13 strain signals from the tower, 8 strain signals from the brakes, 5 crack propagation signals, 25 environmental signals, 22 turbine performance signals and 29 electrical performance signals. All of the rotor instrumentation is described in detail in Sutherland and Stephenson.[3]

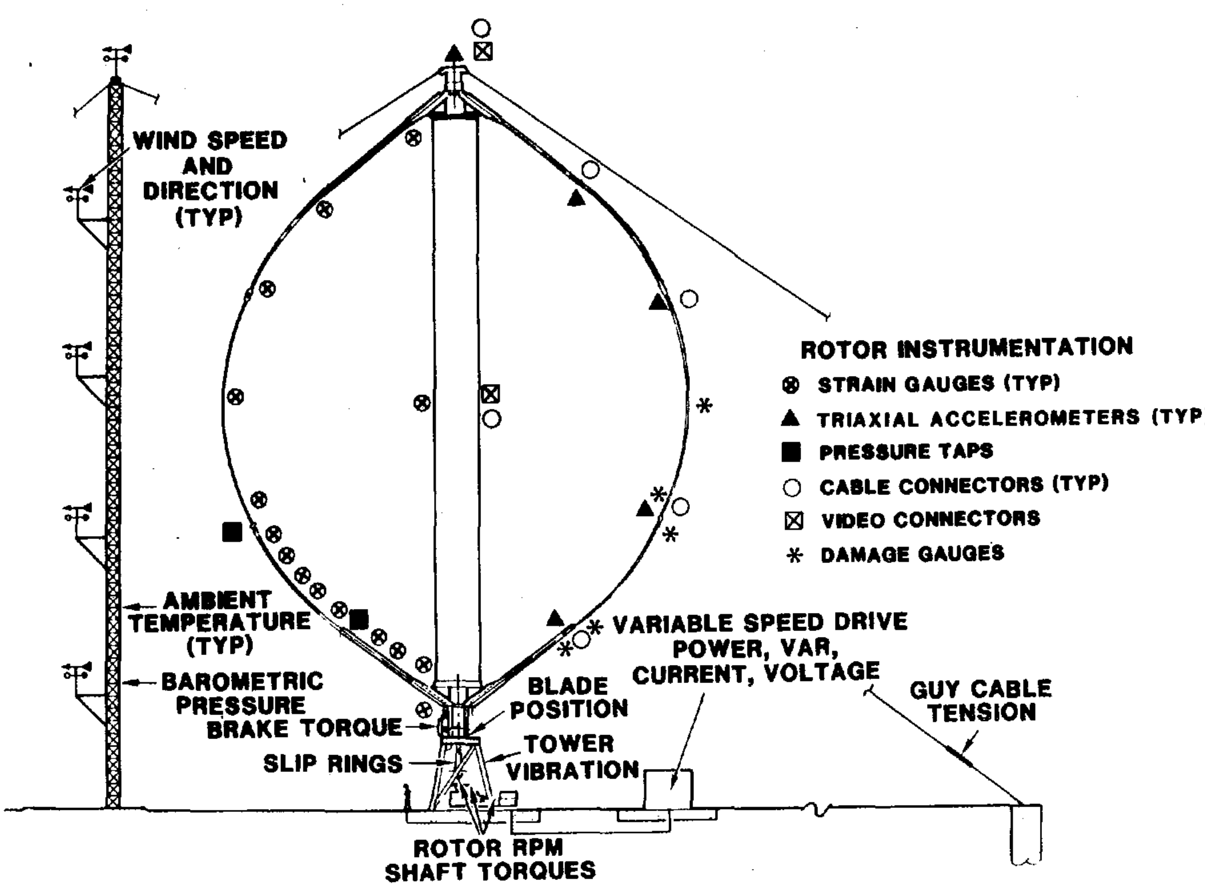

Figure 1. Schematic Diagram of the Test Bed Instrumentation.

This report describes a series of four-point bend experiments that were conducted on each of the machine's ten blade segments. The experiments were designed to validate the readings of the strain gauge circuits placed on the blades. The report begins with a description of the blade strain gauge circuits. The behavior of the blade sections to four-point bending is then analyzed using curved-beam analysis. The experimental procedures are then described and results are compared.

STRAIN GAUGES

The initial set of instrumentation placed on the Test Bed rotor is primarily composed of strain gauges[3] that have been placed strategically about the rotor. In total, 57 gauge circuits were placed on the blades. Major groups of gauges are located about the blade joints and at the equator of the turbine; see Fig 1. Strain gauge categories on the blade include flatwise (spanwise) bending strain, lead-lag (chordwise) bending strain, axial (along the span) strain and total strain. The blade strain gauge circuits are summarized in Appendices A and B.

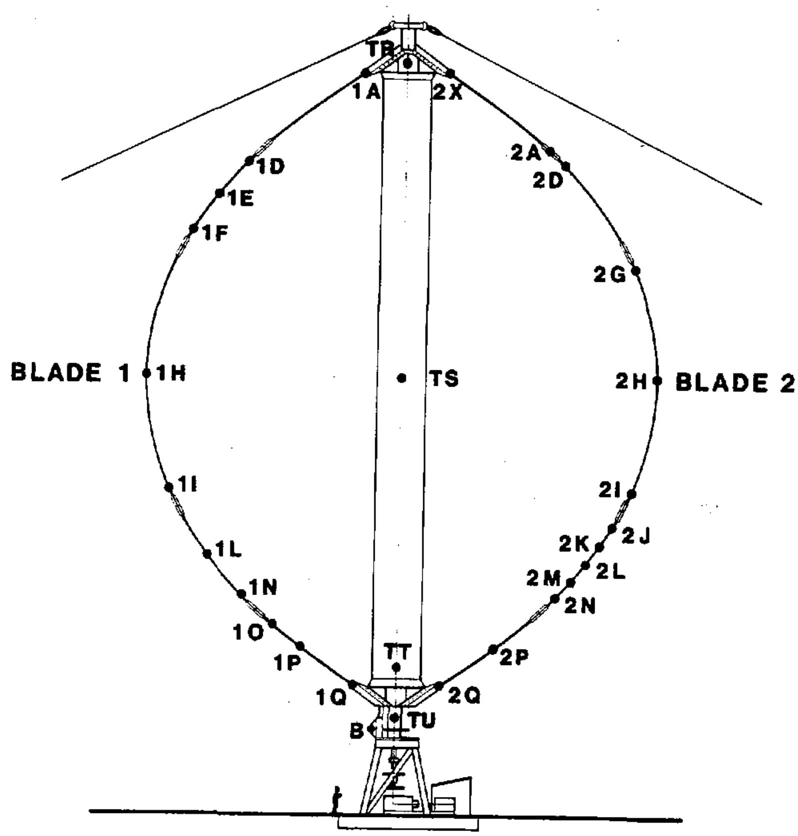

Figure 2. Nomenclature for the Rotor Gauges.

Strain Gauge Descriptors

All strain gauges are designated by their position and their circuit type. The key to the nomenclature for the blade circuits is as follows:

First Letter or Number (see Fig. 2):
- 1 : Blade 1
- 2 : Blade 2

Second Letter or Number (see Fig. 2):
- A through U, and X : Gauge Section

Final Letters or Numbers:
- xxML : Moment Pair in the "Lead-Lag" Position
- xxMF : Moment Pair in the "Flatwise" Position
- xxAL : Axial Pair in the "Lead-Lag" Position
- xxAF : Axial Pair in the "Flatwise" Position

xxDL : Direct Strain in the "Lead-Lag" Position
xxDF : Direct Strain in the "Flatwise" Position
xxF1 : Direct Strain (for the Damage Gauge)

Strain Gauge Circuits

The conventional Wheatstone Bridge circuit[4] was used in this installation for all of the strain gauge circuits. Analysis of the circuit and detailed descriptions of the placement of the various gauges within the circuit are described in Sutherland and Stephenson.[3]

Sign Convention for Stress Measurements

The same sign convention was used for all of the strain gauge circuits. For single gauge configurations and axial pair configurations, tension produces a positive output and compression produces a negative output. For the flatwise bending gauges, tension in the outside fibers (i.e., away from the tower) produces a positive output from the bending gauge circuits (see Fig. 3). For the lead-lag bending gauge circuits, tension in leading edge fibers produces a positive output from the bending gauge circuit (see Fig. 3).

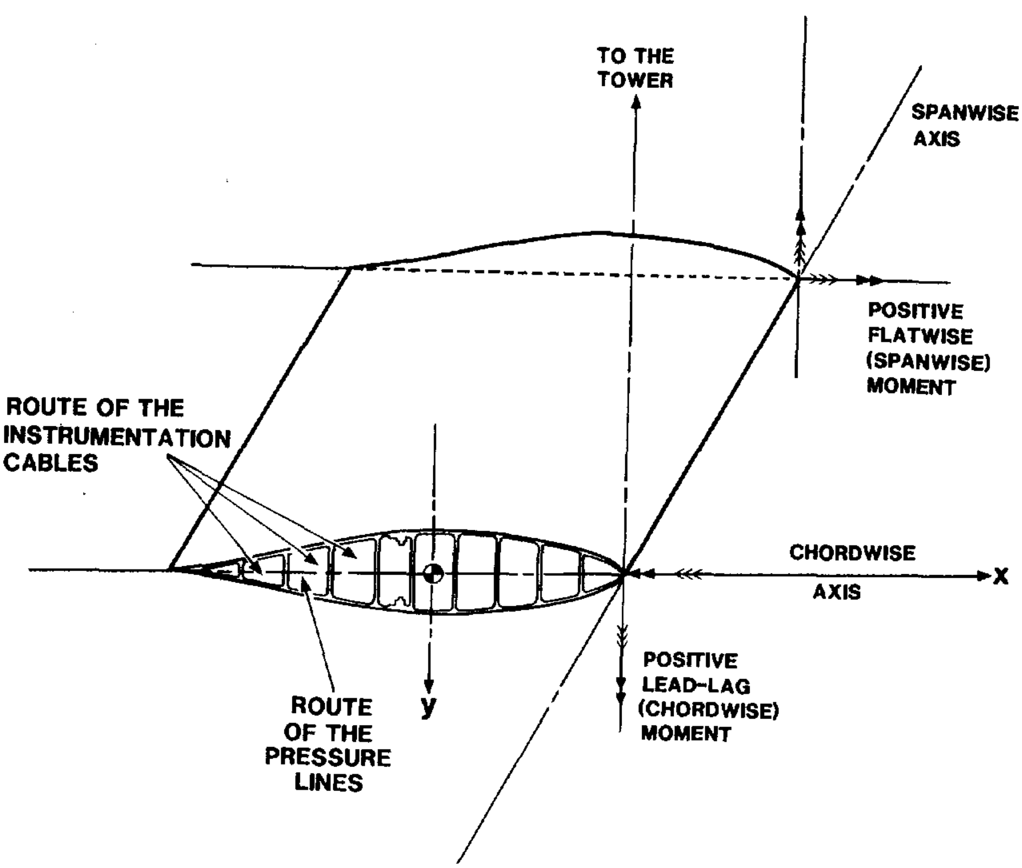

Figure 3. Sign Conventions for the Blade Bending Moments.

Environmental Coating

Coatings of M-Coat D[5] and Hysol EA-960V Fast Room Temperature Curing Adhesive[6] were used to seal the strain gauge circuits from environmental damage and to smooth them and their associated circuitry (e.g., wires, completion units, signal cables and cable risers) into the contour of the blade section. A complete description of the techniques used is given in Sutherland and Stephenson.[3]

Correction Factors

Because of aerodynamic and mechanical restraints, the strain gauges for some circuits had to be placed in positions that precluded measuring "pure" signals. In particular, lead-lag bending circuits have a component of flatwise bending and all of the axial circuits have components of bending. These "cross-talk" terms are analyzed in Sutherland and Stephenson.[3] A synopsis of the analysis presented in that work is repeated here for completeness.

Flatwise Bending: For the flatwise bending circuit, the measured flatwise bending stress equals the maximum flatwise bending stress at that station.

Lead-Lag Bending: For the lead-lag bending circuit, the measured lead-lag bending stress $(\sigma_{lb})_m$ is a function of the flatwise bending stress, σ_{fb}, at the same gauge station. The maximum lead-lag stress σ_{lb} at the gauge station is given by:

$$\sigma_{lb} = \frac{1}{C_{lbl}} (\sigma_{lb})_m + \frac{C_{lbf}}{C_{lbl}} \sigma_{fb} \quad . \quad (1)$$

The values of the cross-talk correction terms, C_{lbl} and C_{lbf}, for the various blade sections are listed in Table I. The other terms in Table I are described below.

Table I. Correction Factors for the Gauge Circuits

Chord Length in	C_{lbl} Eq. (1)	C_{lbf} Eq. (1)	C_{fal} Eq. (2)	C_{laf} Eq. (3)	C_{lal} Eq. (3)
36	0.92768	0.01914	0.18833	0.09660	0.05797
42	0.92645	0.02474	0.20647	0.07447	0.06128
48	0.90311	0.04831	0.43970	0.09792	0.09220

Flatwise Axial: For a flatwise axial circuit, the measured flatwise axial stress $(\sigma_{fa})_m$ is a function of the maximum lead-lag bending stress, σ_{lb}, at the same gauge station. The flatwise axial stress σ_{fa} at the gauge station is given by:

$$\sigma_{fa} = (\sigma_{fa})_m - C_{fal}\, \sigma_{lb} \quad . \quad (2)$$

The values of the cross-talk correction term, C_{fal}, are listed in Table I.

Lead-Lag Axial: For a lead-lag axial circuit, the measured lead-lag axial stress $(\sigma_{la})_m$ is a function of the flatwise bending stress, σ_{fb}, and the maximum lead-lag bending stress, σ_{lb}, at the same gauge station. The lead-lag axial stress, σ_{la}, is given by:

$$\sigma_{la} = (\sigma_{la})_m + C_{laf}\,\sigma_{fb} + C_{lal}\,\sigma_{lb} \qquad . \quad (3)$$

The values of the cross-talk correction terms C_{laf} and C_{lal} are listed in Table I.

EXPERIMENTAL CONFIGURATION

As seen in Fig. 1, each blade is composed of five sections. The cross section of each blade segment is in the shape of an airfoil, see Klimas[2] and Fig. 4. The top and bottom blade sections have an airfoil with a 1.219 m (48 in) chord length; the center section has a 0.914 m (36 in) chord length; and the other two sections have a 1.067 m (42 in) chord length. Here, the blade sections will be identified by their respective chord lengths; namely, 36-inch, 42-inch and 48-inch. References to the upper and lower sections refer to the position of the blade section when mounted on the machine, see Fig. 1.

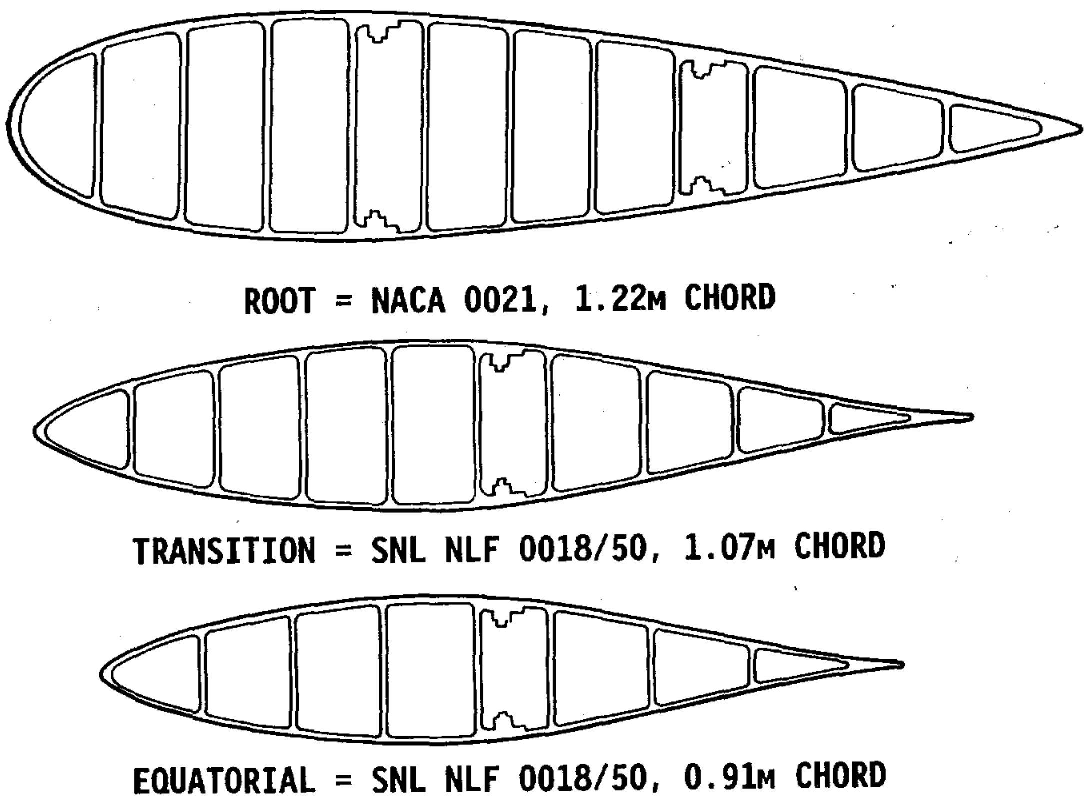

Figure 4. Cross Sectional Views of the Blade Sections.

To validate the response of the strain gauge circuits, each blade section was subjected to a four-point bend experiment. The experimental configuration for these studies is shown schematically in Fig. 5. In this test, the blade section is suspended at each end with a vertical strap, and two weights are hung, symmetrically, about the centerline of the free blade section (i.e., that part of the blade section not enclosed with joint stiffeners). A photograph taken during the bend test of one of the 36-inch chord blade sections is shown in Fig. 6.

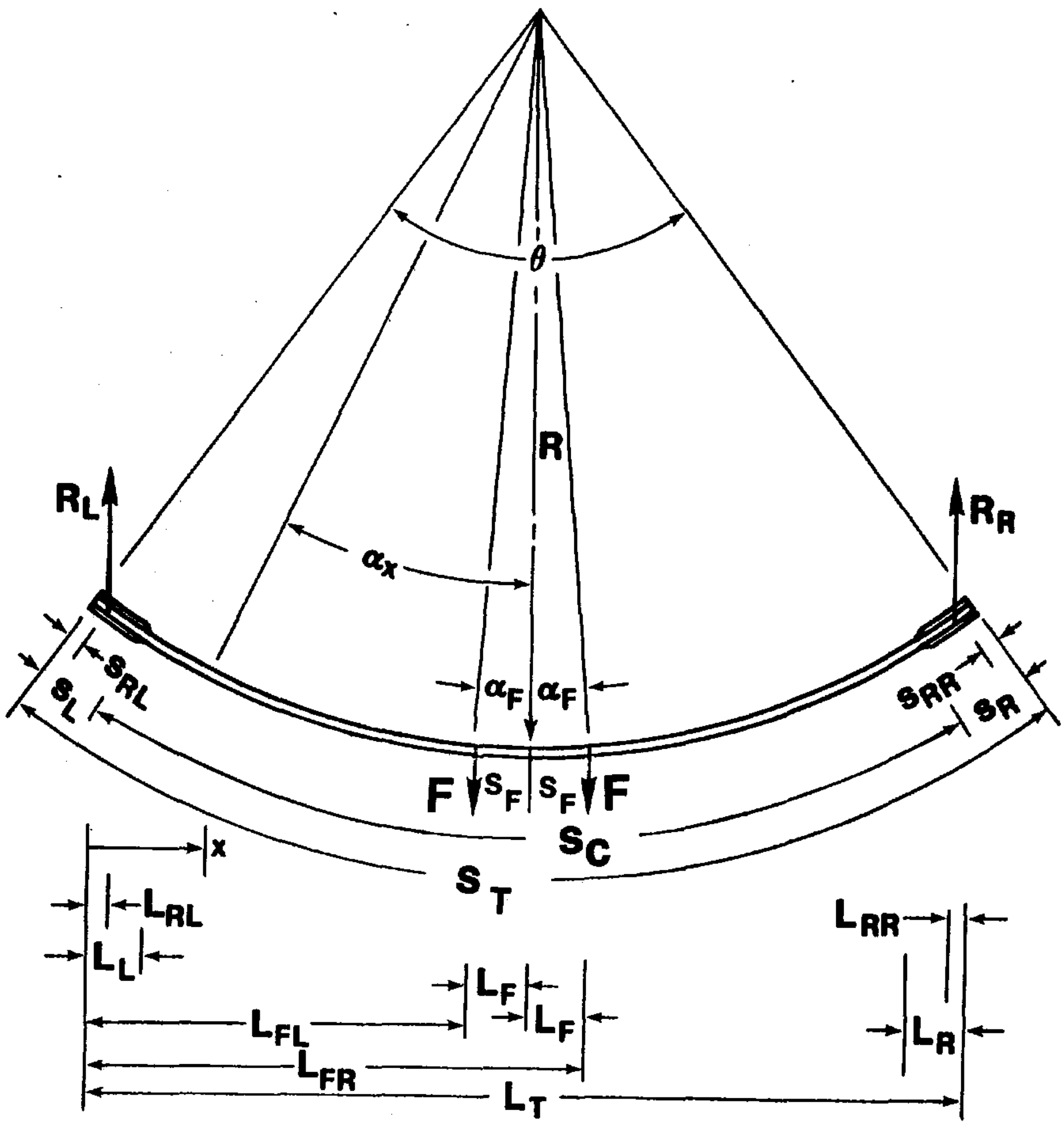

Figure 5. Schematic Diagram of the Four-Point Bend Experiment.

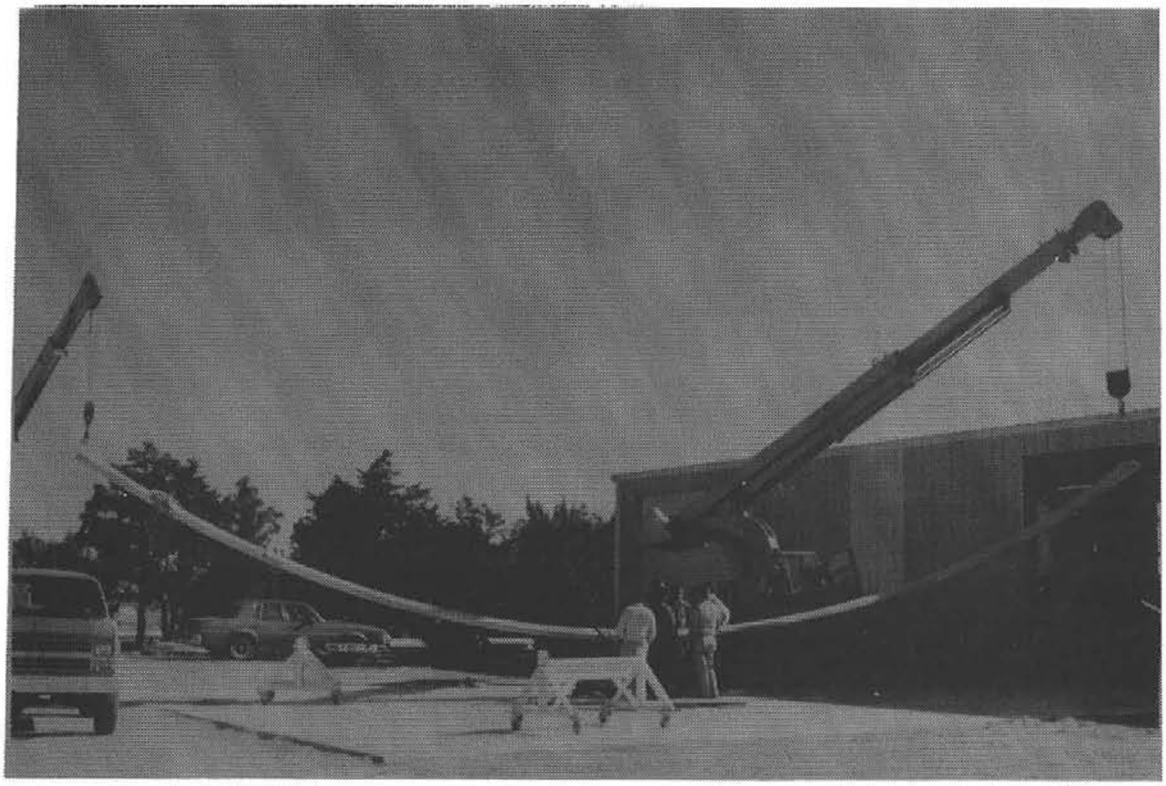

Figure 6. Photograph of the Four-Point Bend Experiment.

Material Properties
A total of 10 blade sections was tested. Each blade section is constructed from 6063 T-6 aluminum. It has an ultimate strength of σ_u of 1.867 MPa (39 ksi), a yield strength σ_y of 1.197 MPa (25 ksi), Young's modulus E of 479 MPa (1.0E7 psi), and Poisson's ration μ of 0.3.

Blade Dimensions
The dimensions of each blade section are shown in Table II. The corresponding sections of each blade have the same length.

Each blade section is reinforced at both ends with aluminum "clam shells" that were machined to the outside contour of the blade. The length of the reinforced section, at all blade-to-blade connections, is 0.610 m (24 in). For the blade-to-tower joint, the length of the reinforced section is 3.05 m (10 ft); see Table II.

The cross sectional bending properties of the blade sections were originally calculated in Ashwill and Leonard[7] and, subsequently, modified by them to reflect changes in the geometry of the cross sections. Their final calculations are summarized in Table III.

Table II. Dimensions of the Blade Sections.

Position	Chord m (in)	Arc Length m (in)	Radius of Curvature m (in)	Reinforcement	
				Top m (in)	Bottom m (in)
Upper	1.219 (48)	10.852 (427.25)	infinite	3.048 (120)	0.610 (24)
	1.067 (42)	7.553 (297.38)	29.87 (1176)	0.610 (24)	0.610 (24)
Center	0.914 (36)	19.133 (753.25)	17.07 (672)	0.610 (24)	0.610 (24)
Lower	1.067 (42)	7.560 (297.63)	29.87 (1176)	0.610 (24)	0.610 (24)
	1.219 (48)	9.211 (362.63)	infinite	0.610 (24)	3.048 (120)

Table III. Cross Sectional Bending Parameters

Chord, m (in)	1.219 (48)	1.067 (42)	0.914 (36)
Area, mm^2 (in^2)	38710 (60.0)	21740 (33.7)	17420 (27.0)
Flatwise Neutral Axis*, mm (in)	128 (5.04)	96.0 (3.78)	82.3 (3.24)
Flatwise Moment of Inertia, m^4 (in^4)	2.425E-4 (582.6)	7.642E-5 (183.6)	4.637E-5 (111.4)
Chordwise Neutral Axis**, mm (in)	553.0 (21.77)	501.7 (19.75)	431.3 (16.98)
Chordwise Moment of Inertia, m^4 (in^4)	4.035E-3 (9695)	1.655E-3 (3976)	9.815E-4 (2358)

* Maximum distance from the blade centerline to the blade surface.
** Distance from the leading edge.

ANALYSIS

Curved Beam Analysis

The four-point bend experiments were analyzed by computing the shear and bending moment diagrams along the length of the each blade section. To compute the stress state at a particular blade location, the analysis assumes that the radius of curvature for the beam is large in comparison to the cross sectional dimensions of the blade. This assumption implies that the bending stresses vary linearly across the cross section of the blade and that simple beam theory may be used to determine the stress state in the blade section. The free body diagram for a section of a curved beam is shown schematically in Fig. 7.

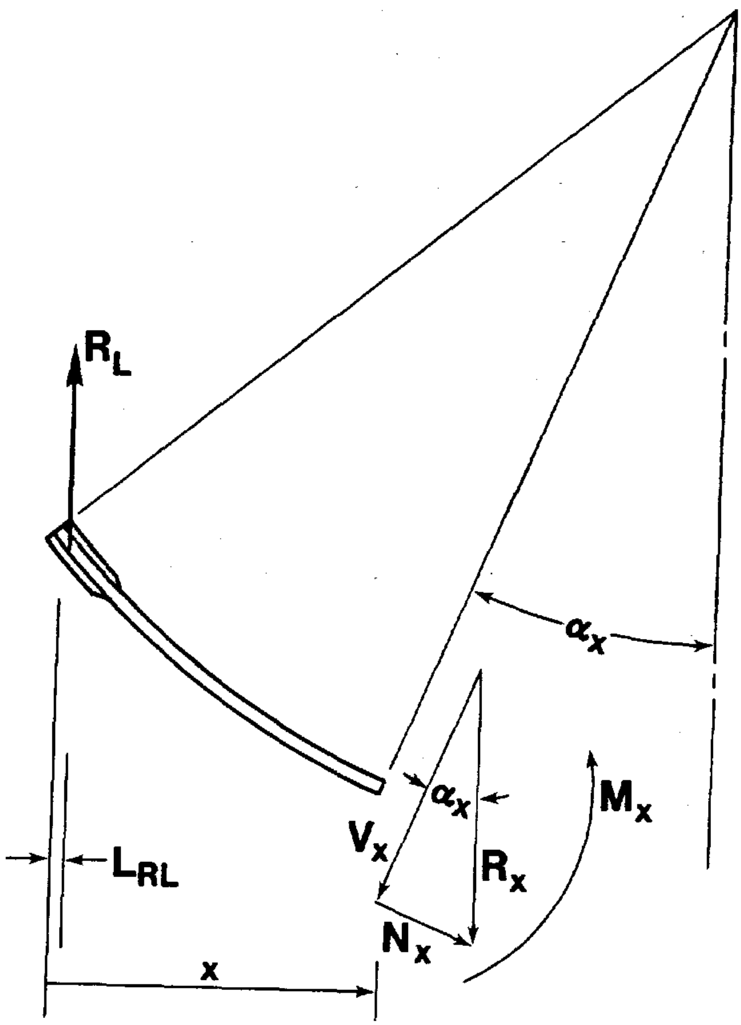

Figure 7. Free Body Diagram for a Curved Beam.

Beam Geometry: As seen in Fig. 5, the total arc length s_T of the blade section is equal to the sum of the arc lengths of the reinforced section on the left end s_L, the center section s_C, and the reinforced section on the right end s_R; i.e.:

$$s_T = s_L + s_C + s_R \quad . \quad (4)$$

For a radius of curvature equal to R, the angle subtended by the total arc is

$$\theta = s_T / R \quad , \quad (5)$$

and the horizontal distance between the ends of the beam L_T is

$$L_T = 2 R \sin(\theta/2) \quad . \quad (6)$$

Applied Forces: Two weights were used to load each blade symmetrically about the centerline of the center section of the blade section, see Fig. 5. The angle α_F from the centerline of the section to these applied forces is

$$\alpha_F = s_F / R \quad , \quad (7)$$

where s_F is the blade length from the centerline to the applied forces.

The horizontal distance from the left end of the beam to the applied force on the left is

$$L_{FL} = (L_T/2) - L_F = (L_T/2) - R \sin(\alpha_F) \quad , \quad (8)$$

where L_F is the horizontal distance from the centerline to the force. From the left end of the beam to the force on the right, the corresponding horizontal distance is

$$L_{FR} = (L_T/2) + L_F = (L_T/2) + R \sin(\alpha_F) \quad . \quad (9)$$

End Reactions: Due to mechanical constraints, the end loads on the blade sections could not be applied at the exact end of the blade section. Rather, they were placed interior to the beam at arc lengths of s_{RL} and s_{RR} from the left and right hand ends of the beam, respectively. L_{RL} and L_{RR} are the corresponding horizontal distances for these arc lengths.

The free body diagram, see Fig. 5, may be solved for the end reactions. The analysis for equal applied loads and $L_{RL} = L_{RR}$ yields:

$$R_L = R_R = F \quad . \quad (10)$$

Reaction Force: Solving the free body diagram for a beam section, Fig. 7, yields a total vertical reaction force R_x at station x of

$$R_x = - R_L\, H(x-L_{RL}) + F\, H(x-L_{FL}) + F\, H(x-L_{FR}) - R_R\, H(x-L_T+L_{RR}) \quad , \quad (11)$$

where $H(\cdot)$ is the Heaviside Step Function. The function R_x is plotted in Fig. 8 for the 36-inch chord section.

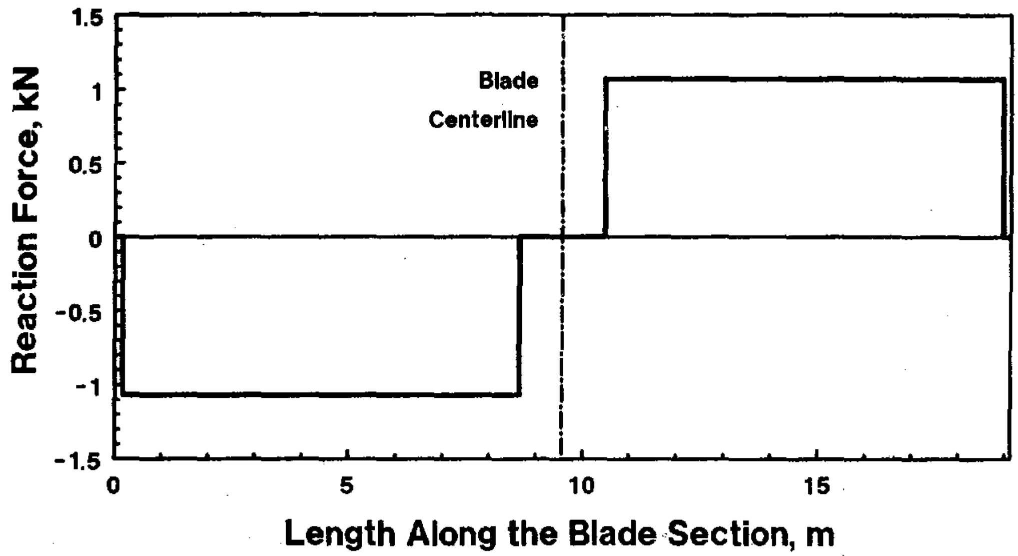

Figure 8. Total Force Diagram for the 36-inch Chord Beam Section.

Shear Force: Solving the vector diagram for the force component parallel to the beam face, see Fig. 7, yields a shear force V_x of

$$V_x = R_x \cos(\alpha_x)$$

$$= - R_L \cos(\alpha_x)\ H(x-L_{RL}) + F \cos(\alpha_x)\ H(x-L_{FL}) + F \cos(\alpha_x)\ H(x-L_{FR})$$

$$- R_R \cos(\alpha_x)\ H(x-L_T+L_{RR}) \quad , \quad (12)$$

where the angle α_x is taken to be the positive angle that is given by

$$\alpha_x = \arcsin\left| \frac{(L_T/2) - x}{R} \right| \quad . \quad (13)$$

The function V_x is plotted in Fig. 9 for the 36-inch chord section.

Normal Force: Solving the vector diagram for the force component perpendicular to the beam face, see Fig. 7, yields a normal force N_x of

$$N_x = - R_x \sin(\alpha_x)$$

$$= + R_L \sin(\alpha_x)\ H(x-L_{RL}) - F \sin(\alpha_x)\ H(x-L_{FL}) - F \sin(\alpha_x)\ H(x-L_{FR})$$

$$+ R_R \sin(\alpha_x)\ H(x-L_T+L_{RR}) \quad . \quad (14)$$

The function N_x is plotted in Fig. 10 for the 36-inch chord section.

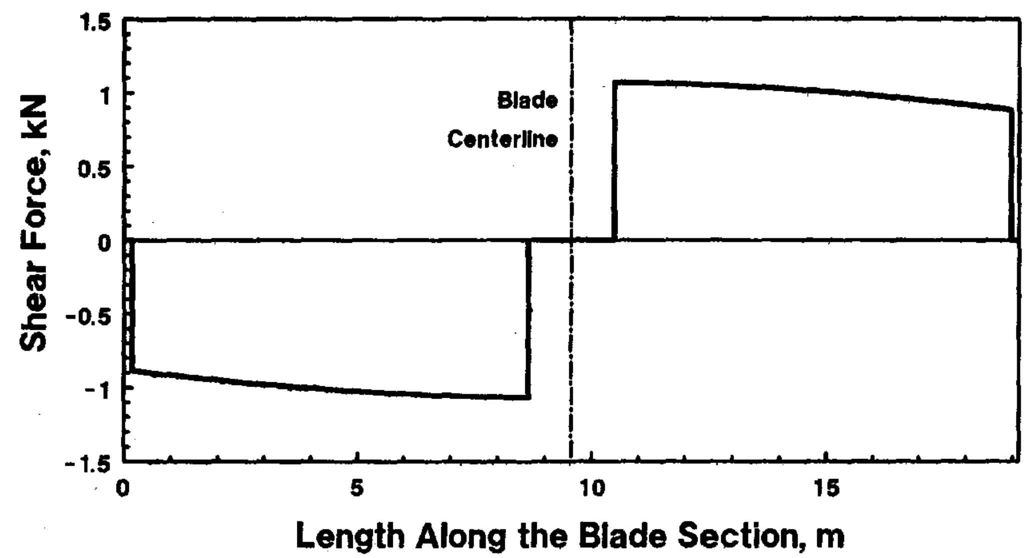

Figure 9. Shear Force Diagram for the 36-inch Chord Beam Section.

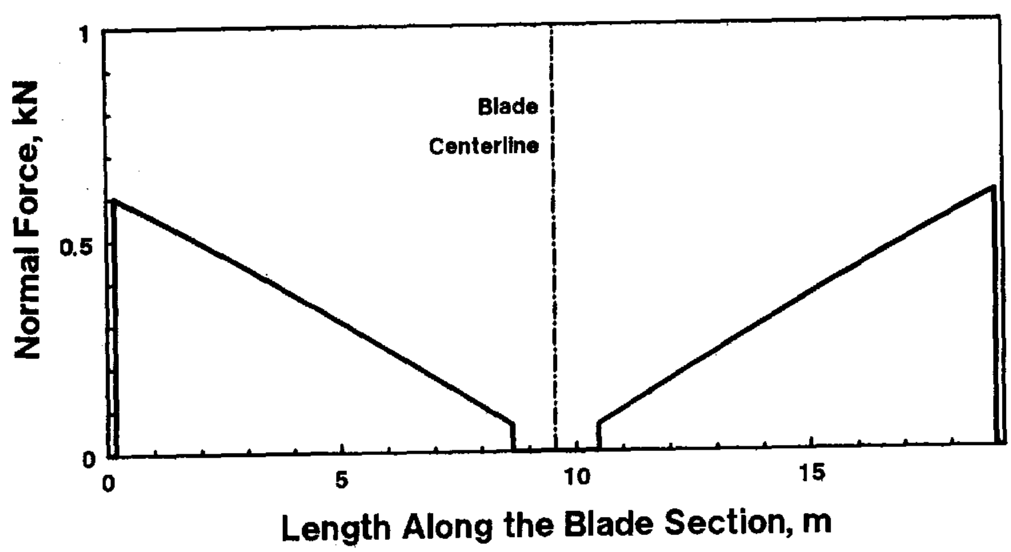

Figure 10. Normal Force Diagram for the 36-inch Chord Beam Section.

Axial Stress: The axial stress can be computed from Eq. (14) by

$$(\sigma_a)_x = N_x / A_x \quad , (15)$$

where A_x is the cross-sectional area of the blade section at station x. The function $(\sigma_a)_x$ is plotted in Fig. 11 for the 36-inch chord section. This function is discontinuous because the cross sectional area varies along the span of the blade section due to the joint reinforcements on each end.

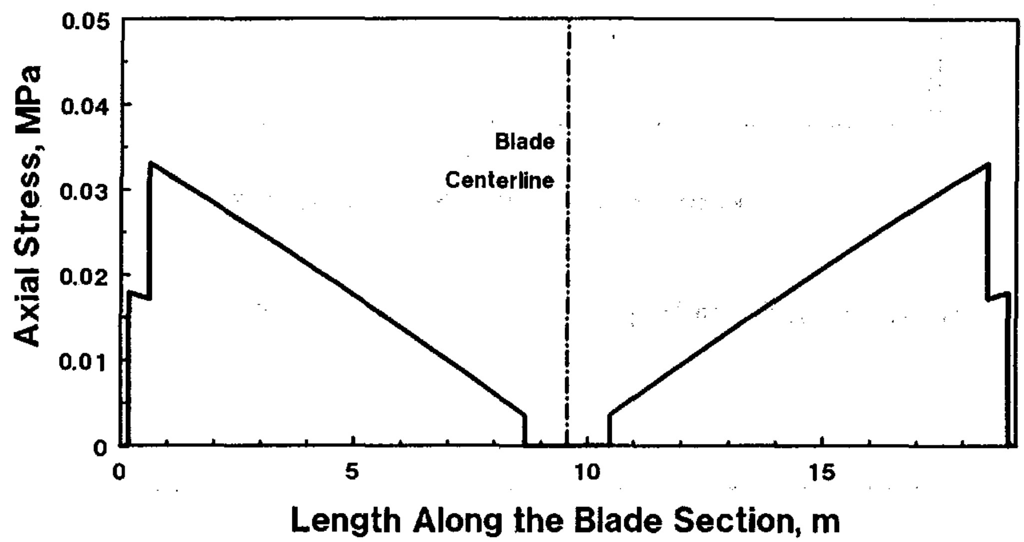

Figure 11. Axial Stress Diagram for the 36-inch Chord Beam Section

Axial Strain: The strain corresponding to the axial-stress component is given by

$$(\varepsilon_a)_x = (\sigma_a)_x / E \quad . (16)$$

This function is plotted in Fig. 12.

Bending Moment: The corresponding bending moment M_x for this beam is

$$M_x = + R_L \, x \cos(\alpha_x) \, H(x-L_{RL}) - F \, (x-L_{FL}) \cos(\alpha_x) \, H(x-L_{FL})$$

$$- F \, (x- L_{FR}) \cos(\alpha_x) \, H(x-L_{FR})$$

$$+ R_R \, (x-L_T+L_{RR}) \cos(\alpha_x) \, H(x-L_T+L_{RR}) \quad . (17)$$

This function is plotted in Fig. 13 for the 36-inch chord section.

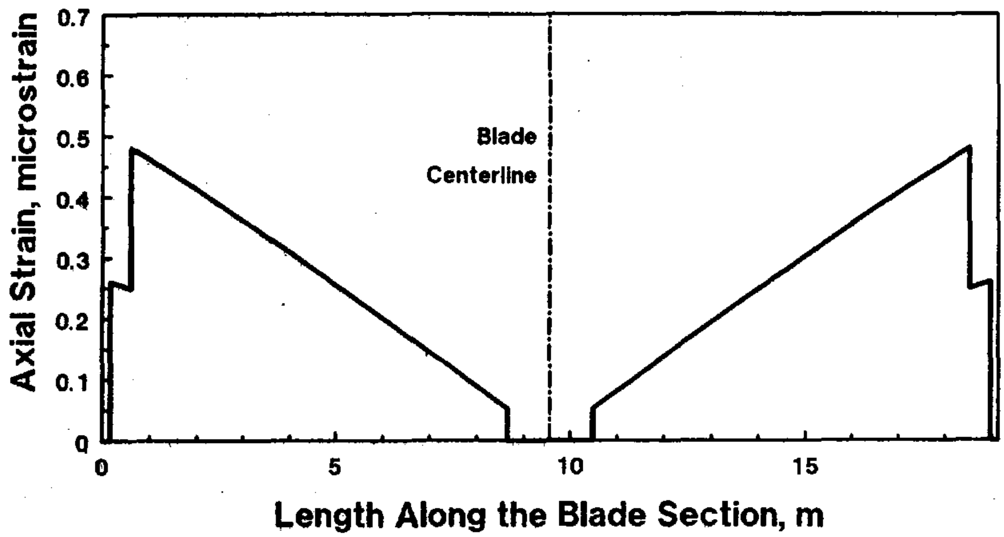

Figure 12. Axial Strain Diagram for the 36-inch Chord Beam Section.

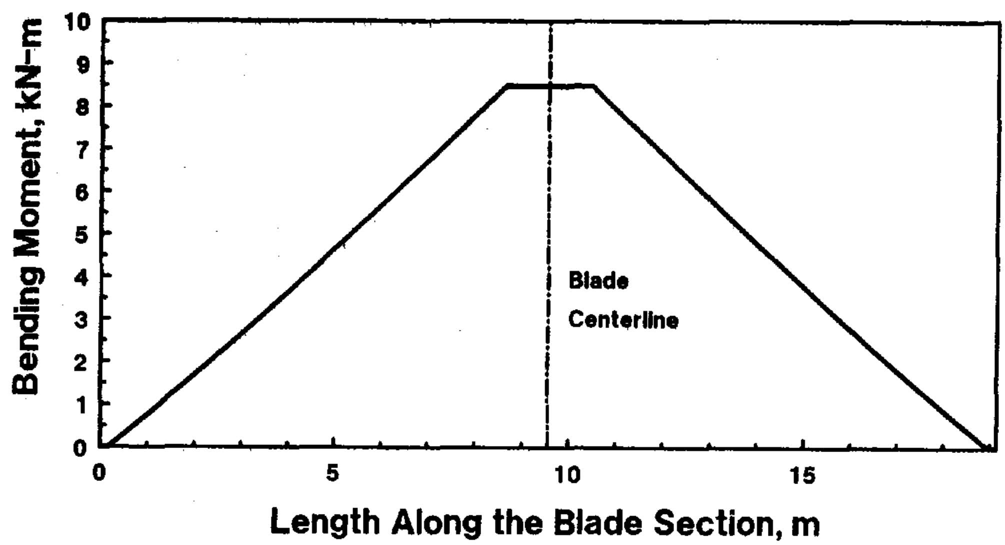

Figure 13. Bending Moment Diagram for the 36-inch Chord Beam Section.

Bending Stress: The assumption of linearity of the bending stress $(\sigma_b)_x$ across the blade section permits the bending stresses to be determined by

$$(\sigma_b)_x = \frac{M_x\, y}{I} \quad , \quad (18)$$

where y is the distance coordinate measured from the neutral axis of the beam and I is the bending moment of inertia of the cross section. The maximum values of y for the three cross sections are listed in Table III. This function is plotted in Fig. 14 for the 36-inch chord section. It is discontinuous because y and I vary along the span of the blade section due to the joint reinforcements on each end.

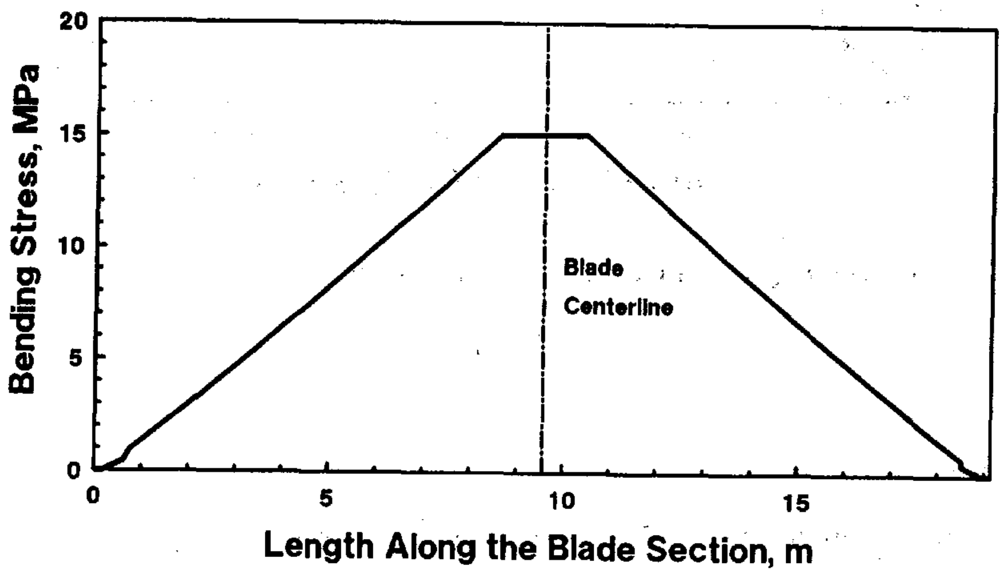

Figure 14. Bending Stress Diagram for the 36-inch Chord Beam Section.

Bending Strain: The corresponding bending strain is given by

$$(\varepsilon_b)_x = \frac{M_x\, y}{E\, I} \quad , \quad (19)$$

where E is Youngs' Modulus for the beam material. This function is plotted in Fig. 15 for the 36-inch chord section.

Straight Beam Analysis

A similar analysis was performed for the straight section of the blade (the four sections with 48-inch cords). Because this analysis repeats the analysis presented above (with R = ∞ and s_L not equal to s_R), the author does not present it here.

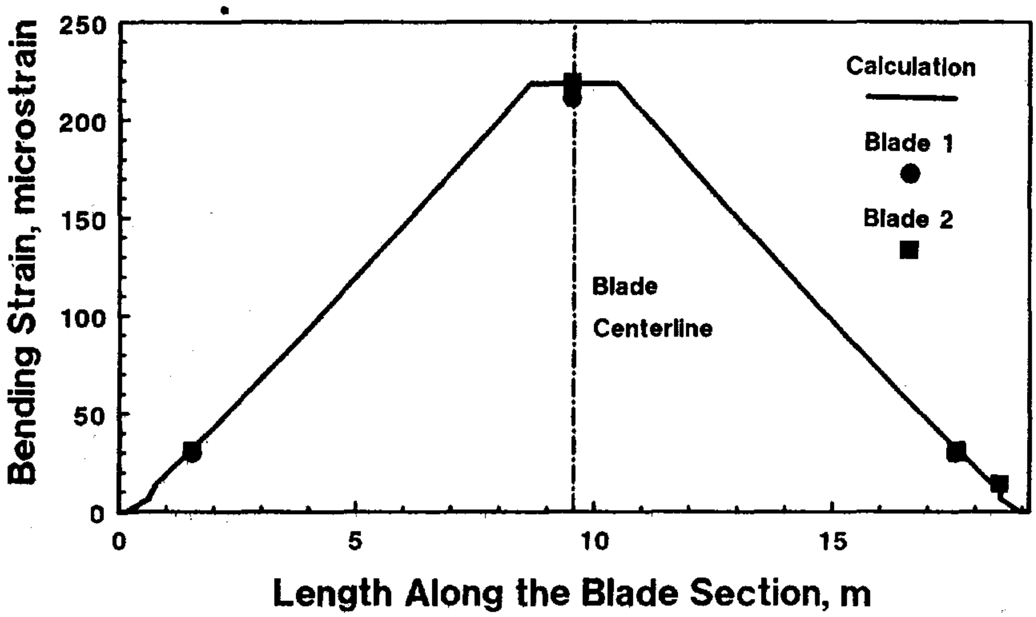

Figure 15. Bending Strain Diagram for the 36-inch Chord Beam Section.

Blade Radius

The strain-gauge readings were referenced to the blade suspended from its ends with no weights suspended from its center; see Reference State below. In this state, the length L_T of each blade section was measured. The lengths of the 42-inch and 48-inch chord blade sections were as predicted by Eq. (6) and the values listed in Table II. However, the lengths of the two 36-inch chord blade sections did not agree with the calculated values. Because the arc length s_T remained unchanged, the radius of curvature must have changed due to gravitation loads imposed on it in the reference state.

The radius of curvature R in the reference state may be determined from Eqs. (5) and (6) using the arc length s_T and the length L_T. The calculation showed that the radius of curvature R decreased from 17.07 m (672 in) in the undeformed state to 15.72 m (619.0 in) in the reference state.

Because this change significantly affected the beam geometry, the analysis cited above was corrected to reflect this change in geometry; i.e., the value of R for the 36-inch chord sections was changed in the analysis from the value cited in Table II to the value cited here.

The value of R decreased further when the concentrated loads were applied. However, this change was small and did not further affect the strain.

Fixture Offset

As described above, the end supports on the blade sections were not attached at the exact end of the blade section. The offset varied for the different sections. For the 36-inch chord section, the horizontal offset was 171.5 mm (6.751 in) at both ends. For the 48-inch chord section, the offset was 88.9 mm (3.50 in) at the both ends. For the 42-inch chord sections, the offset was zero at both ends. This placement of the end loads is reflected by the beginning and trailing unloaded regions shown in Figs. 8 through 15.

EXPERIMENT

A standarized procedure was used to interrogate the strain gauge circuits.[4] Each blade section was placed in its "reference state" and the appropriate wires* were connected to a Vishay Portable Strain Indicator.[8] The circuit-strain reading was then set to zero using the zero adjustment. Then, the blade section was loaded with the appropriate weights, the circuit balanced, and the strains read on the Vishay output dial. The load was then removed and the zero was checked for drift. The strain measurement and zero check were then repeated. All readings were recorded as they were taken. Any discrepancies between the two readings were evaluated and resolved at this time. Three Vishay units were in use; thus, the gauge circuits were measured in groups of three.

The analysis described above was used to predict the strain readings for each circuit before the experiments were conducted. During the course of the experiments, the strain readings were compared to the theoretical predictions. If the measured value did not agree with the prediction, the circuit was retested. If the initial and retest measurements agreed, the original measurement was left unchanged. However, if they did not agree, the initial reading was discarded and replaced with the new measurements. Fewer than five such erroneous readings were found during these experiments.

Based on the multiple readings of each circuit and readings of a calibration circuit, the repeatability of the measurements is estimated to be of the order of ± 3 microstrain.

Reference State

In the analysis presented above, the effects of gravity have been neglected. To eliminate this applied force field from the experiment, the reference state for the strain gauge readings was taken with the blade section suspended from its ends and no weights suspended from its center. The reduced radius of curvature for this stress state was used in the calculations.

Loads

For the 48-inch and 42-inch chord blade experiments, each applied force F was 2.135 kN (480 lb). For the 36-inch chord blade experiments, each F was 1.070 kN (240.5 lb).

---

*The wires for each gauge circuit were contained in the instrumentation cables that were routed through the cells in the blade section. See Sutherland and Stephenson[3] for a complete description of the wiring procedures and cable routes used in this machine.

Encapsulant

The Hysol 960V encapsulant used to protect the strain gauge circuits, see above discussion, has the potential to affect the output of the strain gauge circuits. To address this concern, the strain measurements were conducted twice. The first set of measurements was conducted with no encapsulant covering the gauge circuitry, and the second set was conducted with the gauges encapsulated.

The second set of measurements was also used to determine if the encapsulation process had destroyed the integrity of the strain gauge circuits. One set of broken wires was found. The damaged leads were fixed and then encapsulated again.

RESULTS

The results of the experiments are listed in Appendices C and D for all gauges. The theoretical predictions listed in the appendices have been calculated using Eqs. (16) and (19) and the correction factors cited in Eqs. (1), (2) and (3).

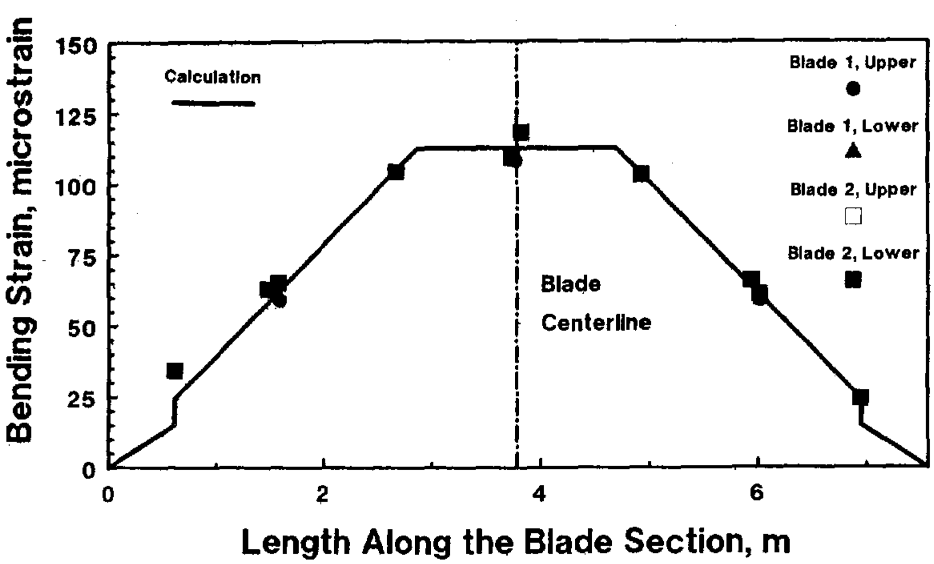

Figure 16. Bending Strain Diagram for the 42-inch Chord Beam Section.

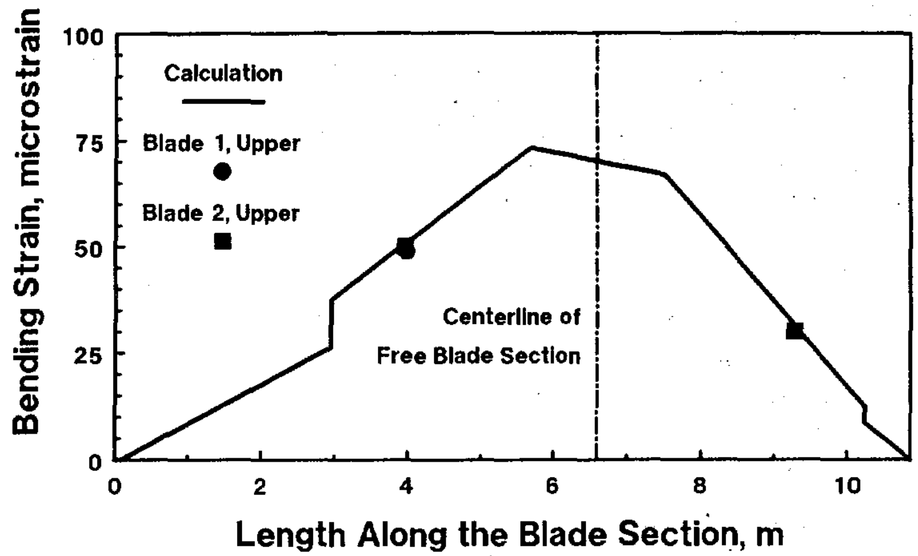

Figure 17. Bending Strain Diagram for the Upper 48-inch Chord Beam Section.

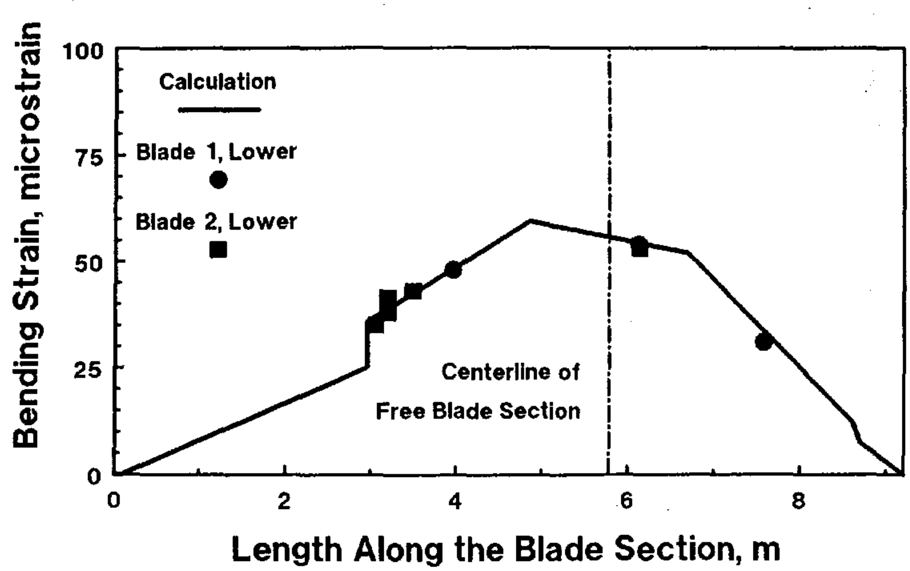

Figure 18. Bending Strain Diagram for the Lower 48-inch Chord Beam Section.

As seen in Appendices C and D, the flatwise bending component is the major strain component in these experiments. The results for this strain component are compared graphically to the theoretical predictions in Figs. 15-18 and are summarized in Appendices E, F and G. In these appendices, "equivalent" gauge sets have been grouped together. Equivalence between gauge circuits is due to the symmetry of the loading for this experiment, the symmetry of the 36-inch and the 42-inch blade sections, the symmetrical placement of gauge circuits on Blade 1 and Blade 2, and the strain state introduced in the beams by this experimental configuration.

Hysol Encapsulant

As seen in Appendices C and D, the gauge readings with and without the Hysol encapsulant are, in general, in very good agreement with one another. The difference between the two gauge readings D_1 is computed as:

$$D_1 = \varepsilon_e - \varepsilon_u \quad , \qquad (20)$$

where ε_u is the strain value measured with no encapsulant (the "None" column in these appendices) and ε_e is the strain value measured with encapsulated gauge circuits (the "Encap" column in these appendices). Fig. 19 presents a distribution plot for D_1. The average value of D_1 is -0.48 microstrain, and the standard deviation is 3.5 microstrain. Both values are of the order of the ± 3 microstrain estimated repeatability of the measurements.

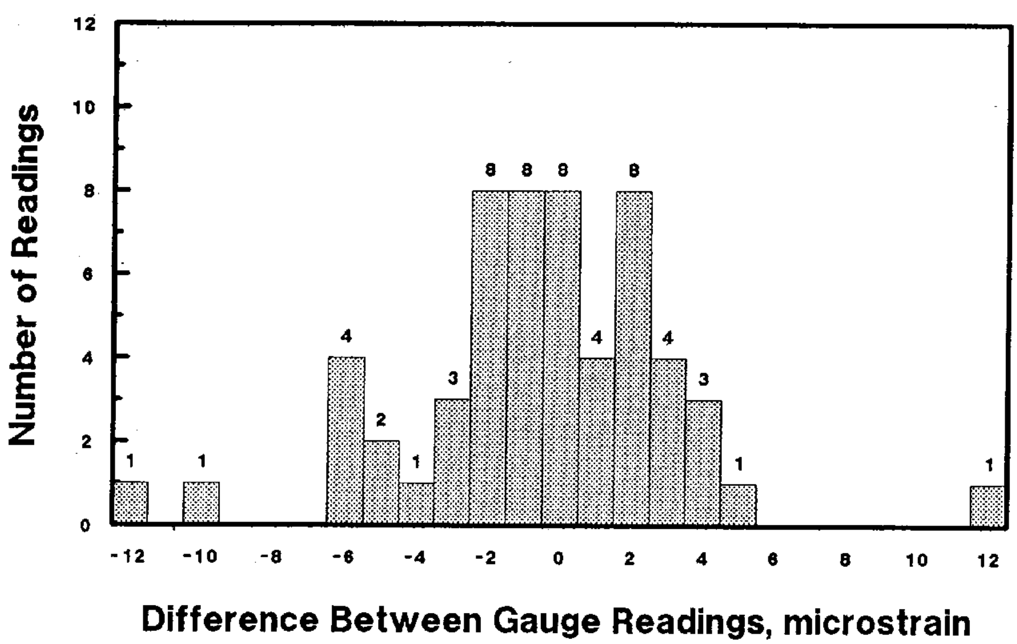

Figure 19. Distribution of the Differences between the Encapsulated and the Unencapsulated Gauge Readings.

As seen in Fig. 19, three gauges lie outside the main group of readings. The gauge circuits are 2LMF, 2LF1 and 2QDF1. The difference values are -12, -10 and +12 microstrain, respectively. These values correspond to -8, -11 and +34 percent deviation, respectively. With the relatively large number of samples reported here (i.e., 57), one would expect, statistically, discrepancies up to 3 or 4 times the estimated repeatability of 3 microstrain. Thus, all of the gauges are in general agreement with one another. However, because these three gauges fall outside the main grouping of the gauge readings, a closer examination of them appears to be warranted.

The discrepancies in the strain readings for gauge circuits 2LMF and 2LF1 can be examined, first, by comparing their readings to equivalent readings. In particular, both circuits are located at the same gauge section, and, for the strain state used in this experiment, their readings should be the same. Moreover, these circuits are equivalent to circuits 1EMF and 1LMF. Comparing these results, see Appendix F, gauges 2LMF and 2LF1 are in agreement with one another but not with 1EMF and 1LMF.

Gauge circuit 2QDF1 can be compared to gauge circuits 1QMF, 2QF1, 2QDF2 and 2QDF3; see Appendix E. This gauge circuit is not in agreement with equivalent gauge circuits. Because this gauge is located 9.5 mm (0.375 in) from the upper end of the blade-to-tower joint, a stress concentration associated with the joint may be affecting the output of this circuit. Because a relatively thick layer of Hysol was used around this joint to smooth it aerodynamically (in addition to encapsulating the gauge circuit), the Hysol could be mitigating the stress concentration during subsequent experiments. The output of this circuit will require continued scrutiny during the course of the test program for the Test Bed.

Another comparison can be obtained by comparing the measured values to the theoretical predictions for this gauge section. In these three cases, the encapsulated gauge readings are closer to the theoretical predictions. Thus, it appears that the gauges were initially reading higher strain than predicted and that they were in better agreement with the theoretical predictions after the encapsulant covered them.

Thus, the Hysol 960V encapsulant has little or no effect on the output of these gauge circuits. Statistical analysis illustrates that the average difference and the standard deviation are of the order of the estimated repeatability of the measurements.

Comparison of Measured and Predicted Strains

As seen in Appendices C and D, the gauge readings with the Hysol encapsulant are, in general, in very good agreement with the theoretical predictions. The difference D_2 between the measured strain with encapsulated gauge circuits and the theoretical prediction for the strain is given by:

$$D_2 = \varepsilon_t - \varepsilon_e \quad , \quad (21)$$

where ε_t is the predicted strain value. Fig. 20 presents a distribution plot for D_2. The average value of D_2 is 0.64 microstrain, and the standard deviation between the readings is 2.5 microstrain. Both are of the order of the ± 3 microstrain repeatability of the measurements and are smaller than that obtained when the before and after encapsulating data are compared.

As illustrated in Fig. 20, all of the gauges have differences between the measured and predicted strain of less than 10 microstrain. Two gauges, 1HMF and 2NDF, have differences of +8 and -8 microstrain, respectively. This difference corresponds to +4 and -31 percent deviation, respectively. As noted above, one would expect, statistically, discrepancies up to 3 or 4 times the estimated repeatability of 3 microstrain. Thus, all of the gauges are in general agreement with the theoretical prediction. Again, as these gauges fall outside the main grouping, a closer examination of them appears warranted.

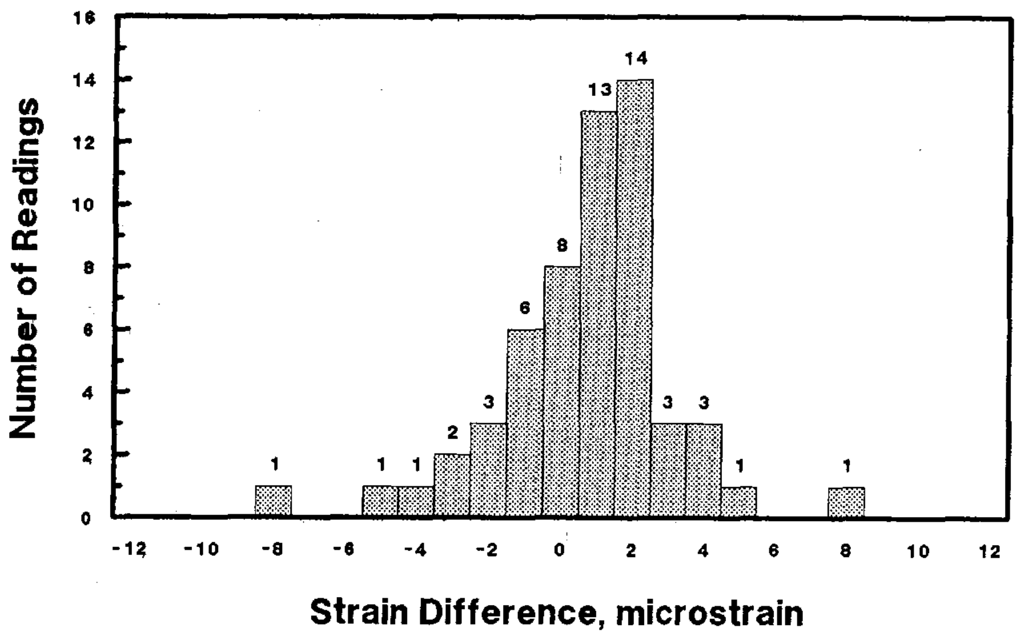

Figure 20. Distribution of the Differences between the Measured and the Predicted Strain Gauge Readings.

Gauge circuit 1HMF can be compared to circuits 2HMF and 2HF1, see Appendix G. As illustrated by this comparison, gauge circuit 1HMF is reading low by a relatively low percentage.

Gauge circuit 2NDF is another gauge that is placed very close to a joint. In this case, the gauges are located 6.4 mm (0.25 in) from a blade-to-blade joint. The stress concentration associated with the joint structure could be causing the high reading. Such a stress concentration would be outside the realm of the linear analysis presented above, and the theoretical prediction would not agree with the measured value. Thus, this gauge will also require close scrutiny during the test program for this machine.

Thus, the theoretical predictions are very close to the strains measured by the gauge circuits after they have been encapsulated. Statistical analysis illustrates that the average difference and the standard deviation are of the order of the estimated repeatability of the measurements.

SUMMARY

The four-point bend experiments conducted here were designed to validate the output of the strain gauge circuits placed on the blades of the Sandia 34-m Test Bed VAWT. Two series of experiments were conducted. The first determined if the gauge circuits were affected by an encapsulant that was used to provide environmental protection and to aerodynamically smooth the circuits into the shape of the airfoil. The second series compared the strain measured by the gauge circuits to theoretical predictions. With only a few noted exceptions, the difference in strain values for a gauge circuit was of the order of the estimated repeatability for the measurement system. Two gauge circuits, 2NDF and 2QDF1, will require continued scrutiny during the course of the test program for the Test Bed. To a lesser extent, gauge circuits 2LMF, 2LF1 and 1HMF will also require scrutiny during the course of the experimental program.

ACKNOWLEDGEMENTS

The author wishes to express his thanks to Ron Davis (USDA, Agricultural Research Service), George Cummings (Missouri Valley Corp.), Larry Schluter (Sandia) and Larry Gallo (Sandia) for their help in conducting the experiments cited in this report.

REFERENCES

1. P. C. Klimas, H. M. Dodd, and R. N. Clark, "An Overview of the DOE/Sandia/USDA Vertical Axis Wind Turbine Test Bed Project," *WindPower 87*, SERI/CP-217-3315, October 1987, pp.35-40.

2. P. C. Klimas, "Sandia National Laboratories 34-Meter Diameter Vertical Axis Wind Turbine Test Bed," *Proceedings of the 1987 ASME Solar Energy Conference*, March 1987, pp. 189-193.

3. H. J. Sutherland and W. A. Stephenson, *Rotor Instrumentation Circuits for the Sandia 34-Meter Vertical Axis Wind Turbine*, SAND88-1144, Sandia National Laboratories, Albuquerque, NM 87185, in publication.

4. R. C. Dove and P. H. Adams, *Experimental Stress Analysis and Motion Measurement*, Merrill Books, Inc., Columbus, 1964.

5. Micro-Measurements Division, Measurements Group, Inc., Raleigh, North Carolina 27611.

6. Hysol Division, The Dexter Corp., 2850 Willow Pass Rd., Pittsburg, CA 94565.

7. T. D. Ashwill and T. M. Leonard, *Developments in Blade Shape Design for a Darrieus Vertical Axis Wind Turbine*, SAND86-1085, Sandia National Laboratories, Albuquerque, New Mexico 87185, September 1986.

8. Vishay Instruments, Vishay International Corp., 63 Lincoln Highway, Malvern, PA 19355.

APPENDIX A

Gauge Circuits for Blade 1

Gauge Desig	Approximate Position			Gauge Configuration
	Blade Section	Position* (in)	From	
1AML 1AMF	Upper 48	37.00 37.00	TOP	Lead-Lag Bending Flatwise Bending
1DML 1DMF	Upper 42	38.5 38.5	TOP	Lead-Lag Bending Flatwise Bending
1EML 1EMF	Upper 42	124.375 124.375	TOP	Lead-Lag Bending Flatwise Bending
1FML 1FMF	Upper 42	36.75 36.75	BOT	Lead-Lag Bending Flatwise Bending
1HML 1HMF 1HAF	Center 36	351.375 351.375 352.125	BOT	Lead-Lag Bending Flatwise Bending Flatwise Axial
1IML 1IMF	Center 36	36.75 36.75	BOT	Lead-Lag Bending Flatwise Bending
1LML 1LMF	Lower 42	123.0 123.0	BOT	Lead-Lag Bending Flatwise Bending
1NML 1NMF	Lower 42	36.0 36.0	BOT	Lead-Lag Bending Flatwise Bending
1OML 1OMF	Lower 48	36.625 36.625	TOP	Lead-Lag Bending Flatwise Bending
1PML 1PMF 1PAL 1PAF	Lower 48	121.25 121.25 121.25 121.25	BOT	Lead-Lag Bending Flatwise Bending Lead-Lag Axial Flatwise Axial
1QML 1QMF	Lower 48	36.0 36.0	BOT	Lead-Lag Bending Flatwise Bending

*The position cited here is the distance from the gauge to the top or bottom of the unreinforced blade section.

APPENDIX B

GAUGE Circuits for Blade 2

Gauge Desig	Approximate Position			Gauge Configuration
	Blade Section	Position (in)	From	
2XML 2XMF	Upper 48	36.0 36.0	TOP	Lead-Lag Bending Flatwise Bending
2AML 2AMF	Upper 48	245.75 245.75	TOP	Lead-Lag Bending Flatwise Bending
2DML 2DMF	Upper 42	37.0 37.0	TOP	Lead-Lag Bending Flatwise Bending
2GML 2GMF	Center 36	36.5 36.5	TOP	Lead-Lag Bending Flatwise Bending
2HML 2HMF 2HF1	Center 36	351.375 351.375 351.375	TOP	Lead-Lag Bending Flatwise Bending Damage Axial
2IML 2IMF 2IDF	Center 36	35.5 35.5 0.313	BOT	Lead-Lag Bending Flatwise Bending Flatwise Total
2JMF 2JF1 2JDF	Lower 42	38.375 34.375 0.25	TOP	Flatwise Bending Damage Axial Flatwise Total
2KMF	Lower 42	81.25	TOP	Flatwise Bending
2LMF 2LF1	Lower 42	122.875 126.5	BOT	Flatwise Bending Damage Axial
2MMF	Lower 42	79.625	BOT	Flatwise Bending
2NMF 2NF1 2NDF 2NML	Lower 42	36.75 39.75 0.25 36.75	BOT	Flatwise Bending Damage Axial Flatwise Total Lead-Lag Bending

APPENDIX B (cont)

Gauge Desig	Approximate Position			Gauge Configuration
	Blade Section	Position (in)	From	
2PMF 2PAL	Lower 48	121.75 121.75	BOT	Flatwise Bending Lead-Lag Axial
2QDF1 2QDF2 2QDF3 2QDL 2QF1	Lower 48	0.375 6.0 17.625 0.375 6.0	BOT	Flatwise Total Flatwise Total Flatwise Total Lead-Lag Total Damage Axial

APPENDIX C

Strain Gauge Readings for Blade 1

Strain Gauge Circuit		Measurements		D_1	Calc	D_2
Gauge	Configuration	None	Encap			
1AML	Lead-Lag Bend	-3	-3	0	-2	1
1AMF	Flatwise Bend	47	49	2	51	2
1DML	Lead-Lag Bend	-2	-4	-2	-2	2
1DMF	Flatwise Bend	60	59	-1	62	4
1EML	Lead-Lag Bend	0	-2	-2	-3	-1
1EMF	Flatwise Bend	108	108	1	112	4
1FML	Lead-Lag Bend	-5	-2	3	-1	1
1FMF	Flatwise Bend	61	59	-3	60	2
1HML	Lead-Lag Bend	-10	-6	4	-4	2
1HMF	Flatwise Bend	215	211	-5	218	8
1HAF	Flatwise Axial	-1	-3	-2	-1	2
1IML	Lead-Lag Bend	-2	-1	2	-1	-0
1IMF	Flatwise Bend	32	30	-2	32	2
1LML	Lead-Lag Bend	-5	-6	-2	-3	3
1LMF	Flatwise Bend	110	108	-2	112	5
1NML	Lead-Lag Bend	-2	-3	-2	-1	2
1NMF	Flatwise Bend	60	59	-2	60	1
1OML	Lead-Lag Bend	-4	-2	2	-2	0
1OMF	Flatwise Bend	35	31	-4	34	3
1PML	Lead-Lag Bend	-3	-3	0	-3	-0
1PMF	Flatwise Bend	54	54	0	54	1
1PAL	Lead-Lag Axial	-5	-5	1	-5	-1
1PAF	Flatwise Axial	0	0	0	-0	-0
1QML	Lead-Lag Bend	-1	-2	-1	-2	-0
1QMF	Flatwise Bend	46	48	2	48	1

APPENDIX D

Strain Gauge Readings for Blade 2

Strain Gauge Circuit		Measurements		D_1	Calc	D_2
Gauge	Configuration	None	Encap			
2XML 2XMF	Lead-Lag Bend Flatwise Bend	-3 50	0 50	3 0	-2 51	-2 1
2AML 2AMF	Lead-Lag Bend Flatwise Bend	-5 30	-1 30	4 1	-2 31	-1 1
2DML 2DMF	Lead-Lag Bend Flatwise Bend	-5 57	-5 59	-1 2	-2 61	3 2
2GML 2GMF	Lead-Lag Bend Flatwise Bend	-4 32	-1 31	3 -1	-1 32	0 1
2HML 2HMF 2HF1	Lead-Lag Bend Flatwise Bend Damage Axial	-8 221 229	-6 215 224	2 -6 -5	-4 218 223	2 4 -1
2IML 2IMF 2IDF	Lead-Lag Bend Flatwise Bend Flatwise Total	-4 30 14	-2 30 14	2 -1 0	-1 31 15	1 2 1
2JMF 2JF1 2JDF	Flatwise Bend Damage Axial Flatwise Total	62 62 24	65 64 24	3 2 0	62 60 26	-2 -4 2
2KMF	Flatwise Bend	100	104	4	105	1
2LMF 2LF1	Flatwise Bend Damage Axial	122 130	110 120	-12 -10	112 115	2 -5
2MMF	Flatwise Bend	109	103	-6	103	0
2NMF 2NF1 2NDF 2NML	Flatwise Bend Damage Axial Flatwise Total Lead-Lag Bend	66 70 33 -2	61 67 34 -2	-6 -3 1 0	60 66 26 -1	-0 -1 -8 1

APPENDIX D (cont)

Strain Gauge Circuit		Measurements		D_1	Calc	D_2
Gauge	Configuration	None	Encap			
2PMF	Flatwise Bend	56	53	-3	54	2
2PAL	Lead-Lag Axial	-1	-2	-1	-5	-3
2QDF1	Flatwise Total	-47	-35	12	-37	-2
2QDF2	Flatwise Total	-43	-38	5	-39	-1
2QDF3	Flatwise Total	-42	-43	-1	-42	1
2QDL	Lead-Lag Total	9	3	-6	5	2
2QF1	Damage Axial	43	42	-1	39	-3

APPENDIX E

Strain Gauge Readings for the 48-inch Chord Blades

Strain Gauge Circuit		Measurements		D_1	Calc	D_2
Gauge	Configuration	None	Encap			
1AMF	Flatwise Bend	47	49	2	51	2
2XMF	Flatwise Bend	50	50	0	51	1
2AMF	Flatwise Bend	30	30	1	31	1
1PMF	Flatwise Bend	54	54	0	54	1
2PMF	Flatwise Bend	56	53	-3	54	2
1OMF	Flatwise Bend	35	31	-4	34	3
1QMF	Flatwise Bend	46	48	2	48	1
2QF1	Damage Axial	43	42	-1	39	-3
2QDF1	Flatwise Total	-47	-35	12	-37	-2
2QDF2	Flatwise Total	-43	-38	5	-39	-1
2QDF3	Flatwise Total	-42	-43	-1	-42	1

APPENDIX F

Strain Gauge Readings for the 42-inch Chord Blades

Strain Gauge Circuit		Measurements		D_1	Calc	D_2
Gauge	Configuration	None	Encap			
1DMF	Flatwise Bend	60	59	-1	62	4
2DMF	Flatwise Bend	57	59	2	61	2
1FMF	Flatwise Bend	61	59	-3	60	2
2JMF	Flatwise Bend	62	65	3	62	-2
2JF1	Damage Axial	62	64	2	60	-4
1NMF	Flatwise Bend	60	59	-2	60	1
2NMF	Flatwise Bend	66	61	-6	60	-0
2NF1	Damage Axial	70	67	-3	66	-1
2JDF	Flatwise Total	24	24	0	26	2
2NDF	Flatwise Total	33	34	1	26	-8
1EMF	Flatwise Bend	108	108	1	112	4
1LMF	Flatwise Bend	110	108	-2	112	5
2LMF	Flatwise Bend	122	110	-12	112	2
2LF1	Damage Axial	130	120	-10	115	-5
2KMF	Flatwise Bend	100	104	4	105	1
2MMF	Flatwise Bend	109	103	-6	103	0

APPENDIX G

Strain Gauge Readings for the 36-inch Chord Blades

Strain Gauge Circuit		Measurements		D_1	Calc	D_2
Gauge	Configuration	None	Encap			
2IDF	Flatwise Total	14	14	0	15	1
1IMF	Flatwise Bend	32	30	-2	32	2
2IMF	Flatwise Bend	30	30	-1	31	2
2GMF	Flatwise Bend	32	31	-1	32	1
1HMF	Flatwise Bend	215	211	-5	218	8
2HMF	Flatwise Bend	221	215	-6	218	4
2HF1	Damage Axial	229	224	-5	223	-1

DISTRIBUTION:

Advanced Alternative Energy
Solutions
5673 W. Las Positas Boulevard
Suite 205
P.O. Box 5246
Pleasanton, CA
Attn: Ugur Ortabasi

Alcoa Technical Center (5)
Aluminum Company of America
Alcoa Center, PA 15069
Attn: D. K. Ai
J. T. Huang
J. R. Jombock
M. Klingensmith
J. L. Prohaska

Alternative Sources of Energy
Milaca, MN 56353
Attn: L. Stoiaken

Amarillo College
Amarillo, TX 79100
Attn: E. Gilmore

American Wind Energy Association
1017 King Street
Alexandria, VA 22314

Dr. A. S. Barker
Trinity Western
7600 Glover Road
Langley, BC
CANADA V3A 4R9

Battelle-Pacific Northwest
Laboratory
P.O. Box 999
Richland, WA 99352
Attn: L. Wendell

Bechtel Group, Inc.
P.O. Box 3965
San Francisco, CA 94119
Attn: B. Lessley

Dr. George Bergeles
Dept. of Mechanical Engineering
National Technical University
42, Patission Street
Athens, GREECE

Bonneville Power Administration
P.O. Box 3621
Portland, OR 97208
Attn: N. Butler

Canadian Standards Association
178 Rexdale Blvd.
Rexdale, Ontario, M9W 1R3
CANADA
Attn: T. Watson

Monique Carpentier
Energy, Mines and Resources
Renewable Energy Branch
460 O'Connor St.
Ottawa, Ontario
CANADA K1A OE4

Professor V. A. L. Chasteau
School of Engineering
University of Auckland
Private Bag
Auckland, NEW ZEALAND

Colorado State University
Dept. of Civil Engineering
Fort Collins, CO 80521
Attn: R. N. Meroney

Commonwealth Electric Co.
Box 368
Vineyard Haven, MA 02568
Attn: D. W. Dunham

M. M. Curvin
11169 Loop Road
Soddy Daisy, TN 37379

Department of Economic Planning
and Development
Barrett Building
Cheyenne, WY 82002
Attn: G. N. Monsson

Otto de Vries
National Aerospace Laboratory
Anthony Fokkerweg 2
Amsterdam 1017
THE NETHERLANDS

DOE/ALO/ETWMD
Albuquerque, NM 87115
Attn: G. P. Tennyson

DOE/ALO
Energy Technology Liaison Office
NGD
Albuquerque, NM 87115
Attn: Capt. J. L. Hanson, USAF

DOE Headquarters (5)
Wind/Oceans Technologies Division
1000 Independence Avenue
Washington, DC 20585
Attn: L. J. Rogers
P. R. Goldman

J. B. Dragt
Nederlands Energy Research
Foundation
(E.C.N.)
Physics Department
Westerduinweg 3 Petten (nh)
THE NETHERLANDS

Electric Power Research Institute
3412 Hillview Avenue
Palo Alto, CA 94304
Attn: E. Demeo
F. Goodman

Dr. Norman E. Farb
10705 Providence Drive
Villa Park, CA 92667

Alcir de Faro Orlando
Pontificia Universidade Catolica-
PUC/Rj
Mechanical Engineering Department
R. Marques de S. Vicente 225
Rio de Janeiro, BRAZIL

Fayette Manufacturing Corporation
P.O. Box 1149
Tracy, CA 95378-1149
Attn: W. Thompson

FloWind Corporation (2)
1183 Quarry Lane
Pleasanton, CA 94566
Attn: L. Schienbein
B. Im

A. D. Garrad
Garrad Hasson
10 Northampton Square
London EC1M 5PA
UNITED KINGDOM

H. Gerardin
Mechanical Engineering Department
Faculty of Sciences & Engineering
Universite Laval-Quebec, GlK 7P4
CANADA

Dr. I. J. Graham
Southern University
Dept. of Mechanical Engineering
P.O. Box 9445
Baton Rouge, LA 70813-9445

R. T. Griffiths
University College of Swansea
Dept. of Mechanical Engineering
Singleton Park
Swansea, SA2 8PP
UNITED KINGDOM

Helion, Inc.
Box 445
Brownsville, CA 95919
Attn: J. Park, President

Indal Technologies, Inc. (2)
3570 Hawkestone Road
Mississauga, Ontario
CANADA L5C 2V8
Attn: D. Malcolm
C. Wood

Institut de Recherche d'Hydro-Quebec
1800, Montee Ste-Julie
Varennes, Quebec, JOL 2P.O.
CANADA
Attn: Bernard Masse

Iowa State University
Agricultural Engineering
Room 213
Ames, IA 50010
Attn: L. H. Soderholm

K. Jackson
West Wind Industries
P.O. Box 1705
Davis, CA 95617

M. Jackson
McAllester Financial
1816 Summit
W. Lafayette, IN 47906

Kaiser Aluminum and Chemical Sales, Inc.
14200 Cottage Grove Avenue
Dolton, IL 60419
Attn: A. A. Hagman

Kaiser Aluminum and Chemical Sales, Inc.
6177 Sunol Blvd.
P.O. Box 877
Pleasanton, CA 94566
Attn: D. D. Doerr

Kansas State University
Electrical Engineering Department
Manhattan, KS 66506
Attn: Dr. G. L. Johnson

R. E. Kelland
The College of Trades & Technology
P.O. Box 1693
Prince Philip Drive
St. John's, Newfoundland, AlC 5P7
CANADA

Kinetics Group, Inc.
P.O. Box 1071
Mercer Island, WA 98040
Attn: J. Sladky, Jr.

KW Control Systems, Inc.
RD#4, Box 914C
South Plank Road
Middletown, NY 10940
Attn: R. H. Klein

L. K. Liljergren
1260 S.E. Walnut #5
Tustin, CA 92680

L. Liljidahl
Building 005, Room 304
Barc-West
Beltsville, MD 20705

Olle Ljungstrom
FFA, The Aeronautical Research Institute
Box 11021
S-16111 Bromma, SWEDEN

Robert Lynette
R. Lynette & Assoc., Inc.
15042 NE 40th Street
Suite 206
Redmond, WA 98052

Massachusetts Institute of Technology
77 Massachusetts Avenue
Cambridge, MA 02139
Attn: Professor N. D. Ham
W. L. Harris, Aero/Astro Dept.

H. S. Matsuda
Composite Materials Laboratory
Pioneering R&D Laboratories
Toray Industries, Inc.
Sonoyama, Otsu, Shiga, JAPAN 520

G. M. McNerney
US Wind Power
160 Wheeler Road
Burlington, MA 01803

Michigan State University
Division of Engineering Research
East Lansing, MI 48825
Attn: O. Krauss

Napier College of Commerce
and Technology
Tutor Librarian,
Technology Faculty
Colinton Road
Edinburgh, EH10 5DT
ENGLAND

National Rural Electric
Cooperative Assn.
1800 Massachusetts Avenue, NW
Washington, DC 20036
Attn: Wilson Prichett, III

Natural Power, Inc.
New Boston, NH 03070
Attn: Leander Nichols

New Mexico Engineering
Research Institute (2)
Campus P.O. Box 25
Albuquerque, NM 87131
Attn: G. G. Leigh
D. Morrison

Ohio State University
Aeronautical & Astronautical Dept.
2070 Neil Avenue
Columbus, OH 43210
Attn: Professor G. Gregorek

Oklahoma State University
Mechanical Engineering Dept.
Stillwater, OK 76074
Attn: D. K. McLaughlin

Oregon State University
Mechanical Engineering Dept.
Corvallis, OR 97331
Attn: R. E. Wilson

Pacific Gas & Electric Co.
3400 Crow Canyon Road
San Ramon, CA 94583
Attn: T. Hillesland

Ion Paraschivoiu
Dept. of Mechanical Engineering
Ecole Polytecnique
CP 6079
Succursale A
Montreal H3C 3A7
CANADA

Jacques Plante
Shawinigan Consultants, Inc.
620 Dorchester Blvd. West
Montreal, Quebec
CANADA H3B 1N8

J. M. Turner Technologies, Inc.
P.O. Box 1058
Schenectady, NY 12301-1058
Attn: Eric N. Hinrichsen

Public Service Co. of New Hampshire
1000 Elm Street
Manchester, NH 03105
Attn: D. L. C. Frederick

Public Service Co. of New Mexico
P.O. Box 2267
Albuquerque, NM 87103
Attn: M. Lechner

RANN, Inc.
260 Sheridan Ave., Suite 414
Palo Alto, CA 94306
Attn: A. J. Eggers, Jr.

Dr. R. Ganesh Rajagopalan,
 Asst. Prof.
Aerospace Engineering Department
Iowa State University
404 Town Engineering Bldg.
Ames, IA 50011

Mr. Bent Rasmussen
Overgade 14
DK-7000 Fredericia
DENMARK

The Resources Agency
Department of Water Resources
 Energy Division
P.O. Box 388
Sacramento, CA 95802
Attn: R. G. Ferreira

Reynolds Metals Company
Mill Products Division
6601 West Broad Street
Richmond, VA 23261
Attn: G. E. Lennox

R. G. Richards
Atlantic Wind Test Site
P.O. Box 189
Tignish P.E.I., COB 2BO
CANADA

Riso National Laboratory
Postbox 49
DK-4000 Roskilde
DENMARK
Attn: Troels Friis Pedersen
 Helge Petersen
 Peter Hauge Madsen

Dr. Ing. Hans Ruscheweyh
Institut fur Leichbau
Technische Hochschule Aachen
Wullnerstrasse 7
FEDERAL REPUBLIC OF GERMANY

Beatrice de Saint Louvent
Etablissement d'Etudes et
 de Recherches Meteorologigues
77 Rue de Serves
92106 Boulogne-Billancourt Cedex
FRANCE

Gwen Schreiner
Librarian
National Atomic Museum
Albuquerque, NM 87185

Arnan Seginer
Professor of Aerodynamics
Technion-Israel Institute of
 Technology
Aeronautical Engineering Dept.
Haifa
ISRAEL

Mr. Farrell Smith Seiler, Editor
Wind Energy News Service
P.O. Box 4008
St. Johnsbury, VT 05819

David Sharpe
Dept. of Aeronautical Engineering
Queen Mary College
Mile End Road
London, E1 4NS
UNITED KINGDOM

Kent Smith
Instituto Technologico Costa Rica
Apartado 159 Cartago
COSTA RICA

Solar Energy Research Institute
1617 Cole Boulevard
Golden, CO 80401
Attn: R. W. Thresher

Bent Sorenson
Roskilde University Center
Energy Group, Bldg. 17.2
IMFUFA
P.O. Box 260
DK-400 Roskilde
DENMARK

Peter South
ADECON
32 Rivalda Road
Weston, Ontario, M9M 2M3
CANADA

Southern California Edison
Research & Development Dept.
Room 497
P.O. Box 800
Rosemead, CA 91770
Attn: R. L. Scheffler

G. Stacey
The University of Reading
Department of Engineering
Whiteknights, Reading, RG6 2AY
ENGLAND

Stanford University
Dept. of Aeronautics and
Astronautics Mechanical Engr.
Stanford, CA 94305
Attn: Holt Ashley

Dr. Derek Taylor
Alternative Energy Group
Walton Hall
Open University
Milton Keynes, MK7 6AA
UNITED KINGDOM

R. Rangi (2)
Low Speed Aerodynamics Laboratory
NRC-National Aeronautical
Establishment
Montreal Road
Ottawa, Ontario, K1A 0R6
CANADA

Texas Tech University
Mechanical Engineering Dept.
P.O. Box 4289
Lubbock, TX 79409
Attn: J. W. Oler

K. J. Touryan
Moriah Research
6200 Plateau Dr.
Englewood, CO 80111

Tulane University
Dept. of Mechanical Engineering
New Orleans, LA 70018
Attn: R. G. Watts

United Engineers and
Constructors, Inc.
P.O. Box 8223
Philadelphia, PA 19101
Attn: A. J. Karalis

Universal Data Systems
5000 Bradford Drive
Huntsville, AL 35805
Attn: C. W. Dodd

University of California
Institute of Geophysics
and Planetary Physics
Riverside, CA 92521
Attn: Dr. P. J. Baum

University of Colorado
Dept. of Aerospace
Engineering Sciences
Boulder, CO 80309
Attn: J. D. Fock, Jr.

University of Massachusetts
Mechanical and Aerospace
Engineering Dept.
Amherst, MA 01003
Attn: Dr. D. E. Cromack

University of Oklahoma
Aero Engineering Department
Norman, OK 73069
Attn: K. Bergey

University of Sherbrooke
Faculty of Applied Science
Sherbrooke, Quebec, J1K 2R1
CANADA
Attn: A. Laneville
P. Vittecoq

The University of Tennessee
Dept. of Electrical Engineering
Knoxville, TN 37916
Attn: T. W. Reddoch

USDA
Agricultural Research Service
Southwest Great Plains Research
Center
Bushland, TX 79012
Attn: Dr. R. N. Clark

W. A. Vachon
W. A. Vachon & Associates
P.O. Box 149
Manchester, MA 01944

Dirk Vandenberghe
State Univ. of Ghent
St. Pietersniewstraat 41
9000 Ghent
BELGIUM

Washington & Lee University
P.O. Box 735
Lexington, VA 24450
Attn: Dr. R. E. Akins

Washington State University
Dept. of Electrical Engineering
Pullman, WA 99163
Attn: F. K. Bechtel

West Texas State University
Government Depository Library
Number 613
Canyon, TX 79015

West Texas State University
Department of Physics
P.O. Box 248
Canyon, TX 79016
Attn: V. Nelson

West Virginia University
Dept. of Aero Engineering
1062 Kountz Avenue
Morgantown, WV 26505
Attn: R. Walters

D. Westlind
Central Lincoln People's
Utility District
2129 North Coast Highway
Newport, OR 97365-1795

Wichita State University
Aero Engineering Department (2)
Wichita, KS 67208
Attn: M. Snyder
W. Wentz

Wind Power Digest
P.O. Box 700
Bascom, OH 44809
Attn: Michael Evans

Wisconsin Division of State Energy
101 South Webster Street
Eighth Floor
Madison, WI 53702
Attn: Wind Program Manager

400	R. C. Maydew
1520	L. W. Davison
1522	R. C. Reuter, Jr.
1522	D. W. Lobitz
1522	E. D. Reedy
1523	J. H. Biffle
1524	A. K. Miller
1524	C. R. Dohrmann
1524	P. S. Veers
1550	C. W. Peterson
1552	J. H. Strickland
1556	G. F. Homicz
3141	S. A. Landenberger (5)
3151	W. I. Klein (3)
3154-3	J. F. Hayes, Actg. (8) For DOE/OSTI (Unlimited Release)
3161	P. S. Wilson
6000	D. L. Hartley
6200	V. L. Dugan
6220	D. G. Schueler
6225	H. M. Dodd (50)
6225	T. D. Ashwill
6225	D. E. Berg
6225	T. C. Bryant
6225	P. C. Klimas
6225	S. D. Nicolaysen
6225	M. E. Ralph
6225	D. C. Reda
6225	M. A. Rumsey
6225	L. L. Schluter
6225	W. A. Stephenson
6225	H. J. Sutherland(10)

7544	D. O. Smallwood
7544	T. G. Carne
7544	J. Lauffer
8524	P. W. Dean